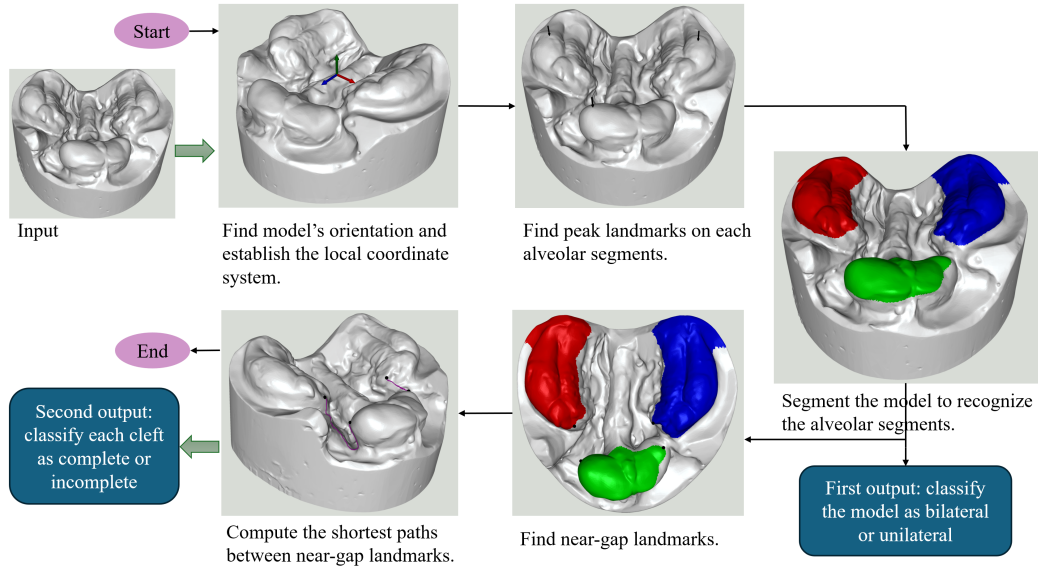


Graphical Abstract

Automatic Classification of Alveolus Clefts on Digital Neonatal Models

Yihang Xie, Grant McLntyre, Peter Mossey, Yang Zhang, Ping Lin



Highlights

Automatic Classification of Alveolus Clefts on Digital Neonatal Models

Yihang Xie, Grant McIntrye, Peter Mossey, Yang Zhang, Ping Lin

- The first fully automatic classification of neonatal alveolar clefts using 3D dental surface models.
- A more robust and accurate method for determining the orientation of dental models.
- Multi-stage region-growing algorithm effectively segments alveolar bone regions.
- Dijkstra's algorithm computes shortest paths to approximate cleft shapes and extent.
- Classifies clefts as unilateral/bilateral and complete/incomplete with high accuracy.

Automatic Classification of Alveolus Clefts on Digital Neonatal Models

Yihang Xie^a, Grant McIntyre^b, Peter Mossey^b, Yang Zhang^c, Ping Lin^{a,*}

^a*School of Science and Engineering, University of Dundee, Nethergate, Dundee, DD1 4HN, United Kingdom*

^b*School of Dentistry, University of Dundee, Netergate, Dundee, DD1 4HN, United Kingdom*

^c*Department of Orthodontics, Affiliated Hospital of Stomatology, Nanjing Medical University, Nanjing, 210029, China*

Abstract

The classification of alveolus clefts in cleft lip and palate clinical cases is a critical prognostic indicator for assessing defect severity and guiding treatment planning. Currently, classification relies on physical examination of the infant's mouth, including visual assessment and palpation to evaluate bone gaps and tissue structures. This manual process is time-consuming, repetitive, and may cause discomfort for infants.

We present a novel automated approach for cleft classification using 3D neonatal dental surface models. The process involves consecutive steps: determining the model's orientation, partitioning and identifying alveolar segments, classifying the model as unilateral or bilateral, capturing the shape of alveolar clefts, and categorizing each cleft as complete or incomplete. We provide examples to illustrate the techniques and discuss the remaining challenges. While our current algorithm focuses on binary cleft classification, it holds promise for more detailed assessments of cleft severity.

Combined with advancements in intra-oral scanning technology, this automated method has the potential to replace labor-intensive and error-prone manual procedures in dental clinics. It represents a significant step towards the automation of routine clinical assessments, improving efficiency, accuracy,

*Corresponding author

Email addresses: 2504171@dundee.ac.uk (Yihang Xie), grant.mcintyre@nhs.scot (Grant McIntyre), p.a.mosse@dundee.ac.uk (Peter Mossey), zyorth@njmu.edu.cn (Yang Zhang), P.Lin@dundee.ac.uk (Ping Lin)

and patient comfort.

Keywords: Alveolar cleft, Dental, 3D analysis, Mesh segmentation, Automation

1. Introduction

Cleft lip and palate (CLP) are the most common craniofacial birth defects in humans, with a global birth prevalence of approximately 1 in 700 live births [1]. Maintaining a registry of children born with CLP is essential for auditing, research, and the effective planning and delivery of services. The use of a standardized classification system, such as the LAHSAL system [2, 3], is critically important for accurately recording cleft types and enabling comparisons across different regions. Despite the recognized value of these systems, there is currently no published literature on the application of artificial intelligence or machine learning to automate cleft classification. This study aims to develop and evaluate a fully automated system for alveolus clefts classification based on the LAHSAL system, utilizing geometric computing and mesh segmentation technology.

Alveolus clefts often co-occur with cleft lip and palate and present as gaps in the upper gum line. These clefts exhibit significant variation in size and morphology between the alveolar bone segments, specifically the premaxilla and maxilla. Classification of alveolus clefts is typically based on completeness and laterality[3, 4, 5] (See Figure 1). Currently, cleft specialists classify a newborn's cleft type through manual and time-consuming processes, including physical examination, visual assessment of cleft characteristics, and sometimes creating physical molds of the oral cavity. This requires inspecting and palpating the alveolar ridge to determine the cleft's completeness and laterality. Manual classification demands substantial expertise, is inefficient, and can cause discomfort for infants, underscoring the need for an efficient, automated method using 3D neonatal dental models. Such a tool would minimize manual intervention, improve accuracy, and enhance patient comfort. Moreover, clinicians and dental researchers could benefit from faster, more objective treatment planning and the ability to efficiently analyze large datasets.

Computer-aided dental treatment has gained considerable attention in recent years, with research focusing on 3D dental models for applications such as tooth segmentation and landmark recognition[6, 7, 8]. However, the

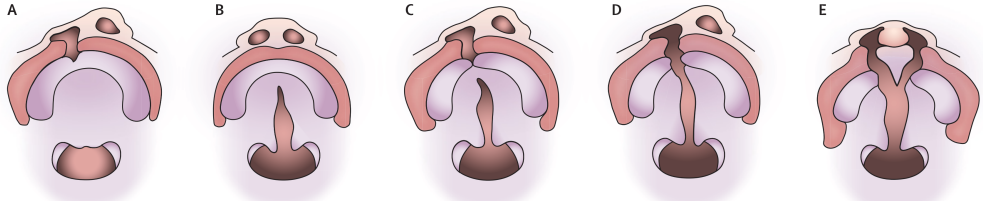


Figure 1: Different cleft lip and palate cases[5]. (A) Cleft lip and alveolus. (B) Cleft palate. (C) Incomplete unilateral cleft lip and palate. (D) Complete unilateral cleft lip and palate. (E) Complete bilateral cleft lip and palate.

application of these technologies to the management of neonatal cleft lip and palate remains limited, largely due to the complex and highly individualized nature of these conditions. This paper addresses the challenges of developing virtual applications for 3D neonatal cleft models and introduces a set of novel techniques designed to overcome these obstacles. These methods, which are not readily available in existing literature, represent a significant advancement in the management of neonatal cleft lip and palate cases, paving the way for more accurate and efficient clinical applications.

2. Related work

The primary challenges in this study are determining the accurate orientation of neonatal dental models and effectively segmenting and recognizing alveolar segments. Therefore, we discuss general orientation and mesh segmentation methods, as well as techniques specifically developed for this study. Then, Dijkstra’s shortest path algorithm, especially in the context of alveolar cleft classification, is introduced.

2.1. Orientation techniques

The orientation of dental models is fundamental to our algorithm, as it is essential for locating predefined landmarks, such as the highest point (peak) on each alveolar segment. Various methods exist for addressing the orientation of 3D dental models. Some studies, such as Kumar et al.[9], assume that all models are pre-oriented in a uniform manner and thus do not address orientation variability. Ma et al.[10] employ the least squares method to establish a reference horizontal plane by fitting the teeth mesh data, thereby determining the model’s orientation via the plane and its normal vector.

The most commonly used technique is principal component analysis (PCA), which heuristically and automatically generates three axes to define a model’s orientation [8, 11]. PCA is both efficient and easy to implement. You can find an available implementation in any programming language online.

Initially, we explored the use of PCA to orient neonatal cleft models. However, this method proved less effective for these models, as illustrated in Figure 16. The complexity and irregular distribution of the point clouds in cleft neonatal models hindered PCA. Instead, we consider the overall shape of the dental model. By fitting a minimum-volume bounding box around the model, we establish its orientation based on the box’s center and orientation axes. This method produces significantly more accurate results compared to PCA when applied to neonatal models.

The orientation of the dental model in our study is determined by computing its 3D oriented bounding box (OBB), a widely used technique in computer graphics. The most accurate algorithm for calculating a 3D OBB, introduced by O’Rourke in 1985[12], is computationally intensive and too slow for real-world applications. Consequently, most modern methods approximate the OBB. Gottschalk et al.[13] utilizing PCA and 3D model’s convex hull to heuristically generate OBB’s axes. Barequet and Har-Peled[14] introduced a brute-force approach that evaluates a large set of candidates to find the one with the smallest volume. Chang et al.[15] developed a hybrid optimization method that is faster and more reliable than other state-of-the-art techniques.

Despite the accuracy of OBB, it is extremely challenging to implement [13, 14, 15]. For our neonatal dental models, we adopted Chang’s method, available through the computational geometry framework CGAL [16]. This approach was chosen for its combination of efficiency, accuracy, and the availability of a robust implementation, making it particularly well-suited to the requirements of our study.

2.2. Mesh segmentation techniques

Mesh segmentation is essential for identifying significant components within a 3D mesh model. Research in this field has led to two principal methodologies: traditional rule-based approaches and modern data-driven techniques. Recently, data-driven methods have gained prominence due to advancements in machine learning [17, 18]. However, given the limited availability of infant cleft digital models, this study focuses on traditional geometric segmentation methods.

Traditional segmentation strategies are broadly classified into cluster-based and boundary-based methods. Cluster-based techniques partition a mesh by grouping its elements—vertices, edges, or faces—whereas boundary-based methods delineate segment boundaries or contours as a connected sequence of edges and vertices, without considering interior elements [19]. The substantial variation in cleft shapes across clinical cases complicates the establishment of a standardized boundary metric for the alveolar bone. Therefore, cluster-based methods, specifically region-growing[20] and watershed[21] algorithms, are more appropriate for this study. Inspired by Woodsend et al. [8], who successfully applied a region-growing method with curvature as a stopping criterion to segment individual teeth, we adopt a similar approach but employ an alternative stopping criterion tailored to segment the alveolar bone effectively.

The region-growing method is a computational geometry technique used for dividing a mesh into several segments. This process begins with a selected initial point—either a vertex or a polygon—known as a seed, and expands to include adjacent elements. The expansion continues until it meets a pre-defined condition, known as a stopping criterion ([20] provides an in-depth discussion). The uniqueness of any region-growing method lies in the specific criteria it uses for incorporating new elements into a region.

In this paper, we segment the alveolar bone to recognize the count and location of the alveolar cleft between segments. Segmenting the alveolar bone poses unique challenges compared to individual tooth segmentation. While tooth boundaries can be effectively captured by the curvature field, forming a concave contour between the teeth and gum [8, 11, 22], the alveolar bone lacks clear contours to distinguish its segments (See Figure 2). In earlier phases of this study, we attempted to define the shape and boundary of each alveolar segment but found it challenging to establish a consistent rule based on geometric features to precisely capture segment boundaries. Consequently, we could only shift our approach to approximate the shape of each alveolar segment and focus on identifying segment count and gap locations.

2.3. Dijkstra’s shortest path algorithm

Dijkstra’s algorithm is a well-established method in computational geometry for finding the shortest path between nodes in a graph[23]. The implementation of the algorithm is directly available in any common programming environment. In the context of 3D modeling, Dijkstra’s algorithm has been adapted to calculate the shortest paths on polygonal meshes, where

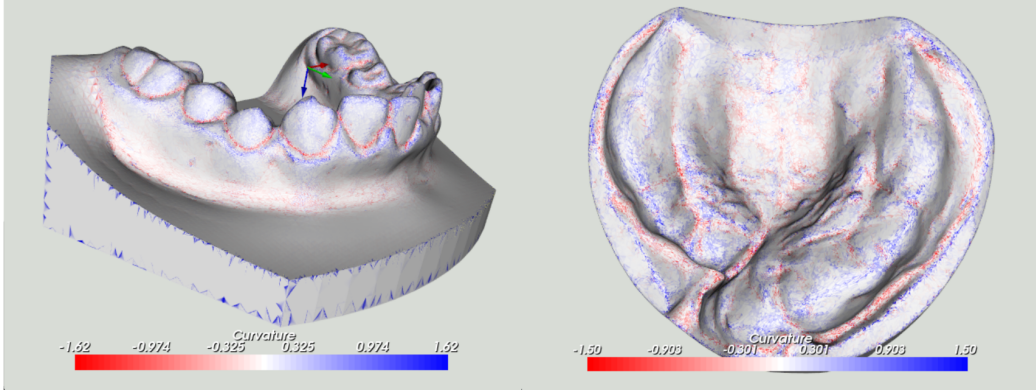


Figure 2: Signed curvature field on adult teeth model (left) and neonatal cleft model (right)– Notice the ring of red along the tooth-gum join surrounding each tooth and between neighbouring teeth

vertices or triangles represent graph nodes, and edges define connections between them. By assigning weights to edges based on their Euclidean distances or other geometric properties, the algorithm efficiently computes paths that adhere to the mesh’s surface, making it ideal for applications requiring surface-based pathfinding.

In this study, Dijkstra’s algorithm plays a pivotal role in approximating the geometric features of clefts between alveolar segments. By identifying the shortest path between landmarks located near cleft regions, the algorithm provides a reliable representation of the cleft’s shape. This representation is crucial for distinguishing between complete and incomplete clefts, as well as for assessing the spatial relationships between alveolar segments.

3. Materials and Methods

Since alveolar clefts occur in different sizes and shapes, careful and comprehensive selection of test datasets is necessary in cleft classification studies. We evaluated 17 neonatal upper jaw models (See Table 1) with varying levels of complexity and detail. For example, models with an associated palate cleft are typically more severe and complex than those without one. The models were acquired using 3D dental scanners or intra-oral scanners. Manufacturer-supplied software preprocessed each dental mesh to ensure they were manifold and non-degenerate. These models, stored in STL format, provide the basis for our evaluation.

Count	Qualifiers	
5	Unilateral	1 incomplete cleft
6	Unilateral	1 complete cleft
4	Bilateral	2 complete clefts
2	Bilateral	1 complete cleft and 1 incomplete cleft

Table 1: Types and counts of models used in this study.

STL files, distinct from other 3D formats, are exclusively designed to describe the surface geometry of three-dimensional objects, omitting any color or texture information. In this research, STL files are processed through a half-edge Mesh[24] - a sophisticated data structure in computer graphics that efficiently represents 3D polygonal meshes. This structure offers enhanced efficiency and simplifies interactions with the mesh’s structural and connective properties. It is important to note that while STL files typically lack inherent scale information, with units often being arbitrary, the dental scans in this study consistently use millimeters as the unit of measurement to ensure precision and uniformity.

These dental mesh models are taken as input of the proposed algorithm as demonstrated in Figure 3, and the output classifications identify each model as bilateral or unilateral, and as incomplete or complete.

3.1. Find orientation

Before analysis, we must establish the model’s orientation because different scanners use varying conventions, and initial orientations are often inaccurate. Therefore, it is crucial for the system to detect and normalize the models’ orientation internally before further analysis.

Determining orientation in dental scans involves creating a local coordinate system where the basis vectors represent approximate directions—*right*, *forward*, *up*—within the model (See Figure 4). These basis vectors—denoted as \vec{u}_{right} , \vec{u}_{up} , and \vec{u}_{forward} —provide only an approximation, as defining exact unit vectors for these directions is challenging. When inspecting a vertex, these vectors should be used to negate the effects of the model’s position and pose. For example, to determine a vertex’s height, the inner product of the vertex and the *up* vector should be used instead of relying on raw Y-coordinate values.

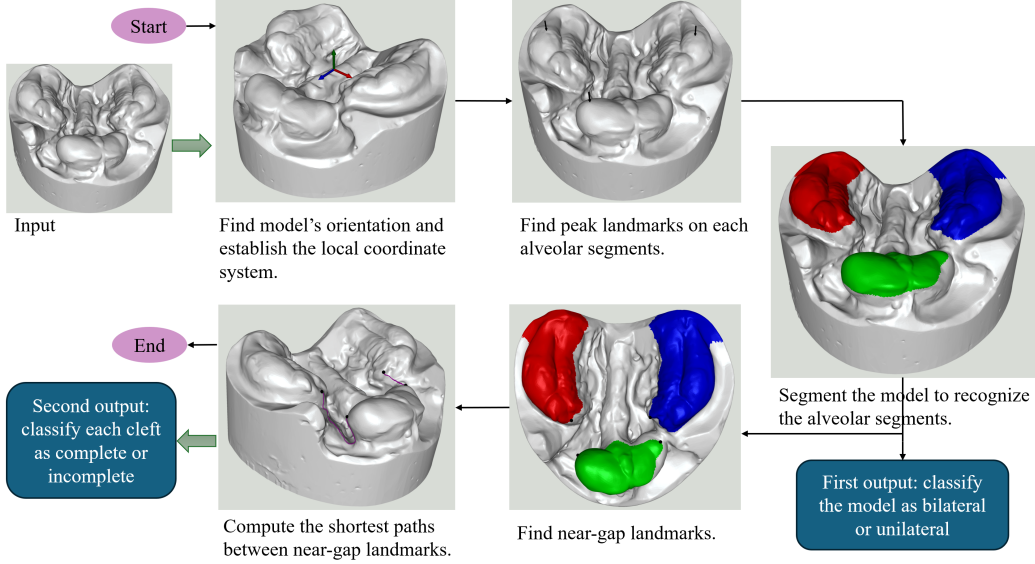


Figure 3: Flowchart summary of automatic cleft classification process

3.1.1. Oriented bounding box

An Oriented Bounding Box (OBB) for a three-dimensional object is defined as the box with the smallest volume that encompasses all points of the object, as illustrated in Figure 5. To minimize volume, the box must fit the model as closely as possible, making the OBB ideal for generating a local coordinate system for dental models. For details on OBB calculation, see [15], and for an available implementation, refer to [16].

In a typical dental model, the width (left/right) is greater than the length (forward/backward), and the length is greater than the height. Therefore, the longest edge of the OBB represents the *left/right* direction, the second longest represents the *forward/backward* direction, and the shortest represents the *up/down* direction.

3.1.2. Sign of the unit vectors

After obtaining the OBB of a dental model, we derive three unit vectors representing the *left/right*, *forward/backward*, and *up/down* directions. However, the initial signs of these vectors are arbitrary and must be adjusted to align with the desired coordinate system. This adjustment involves verifying and, if necessary, reversing the vector directions to accurately establish the basis vectors for the intended coordinate system. The following checks were

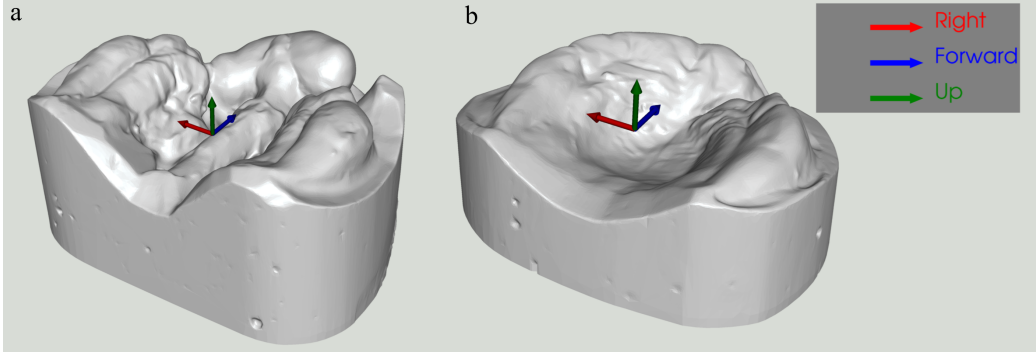


Figure 4: Local coordinate system of two cleft models

adopted (in the following order).

1. **Up/Down:** Verifying the up/down direction is straightforward. Since the occlusal surface has the highest triangle density, the average normal of all triangles should approximately point upward. The OBB's up direction should then be adjusted to match this approximate upward direction.
2. **Forward/Backward:** To determine the forward/backward direction, we project all vertices of the model onto the horizontal plane, capturing an approximate arch shape of the alveolar bone. Each vertex is weighted by the inner product of its position and the previously determined up direction, emphasizing vertices on the alveolar bone. A weighted quadratic curve is then fitted to these horizontal components. If the forward vector's sign is correct, the quadratic curve should form a \cap shape with a negative x^2 coefficient (See Figure 6).
3. **Right/Left:** Given that the coordinate system is designed as a right-handed system and the directions of the other two axes are known, we can determine the correct leftward direction by performing the cross product of \vec{u}_{up} , and \vec{u}_{forward} :

$$\vec{u}_{\text{right}} = \vec{u}_{\text{up}} \times \vec{u}_{\text{forward}} \quad (1)$$

3.2. Find peaks

Peaks are defined as landmarks located on alveolar segments, where each peak represents the highest point on an alveolar segment. Since the alveolar

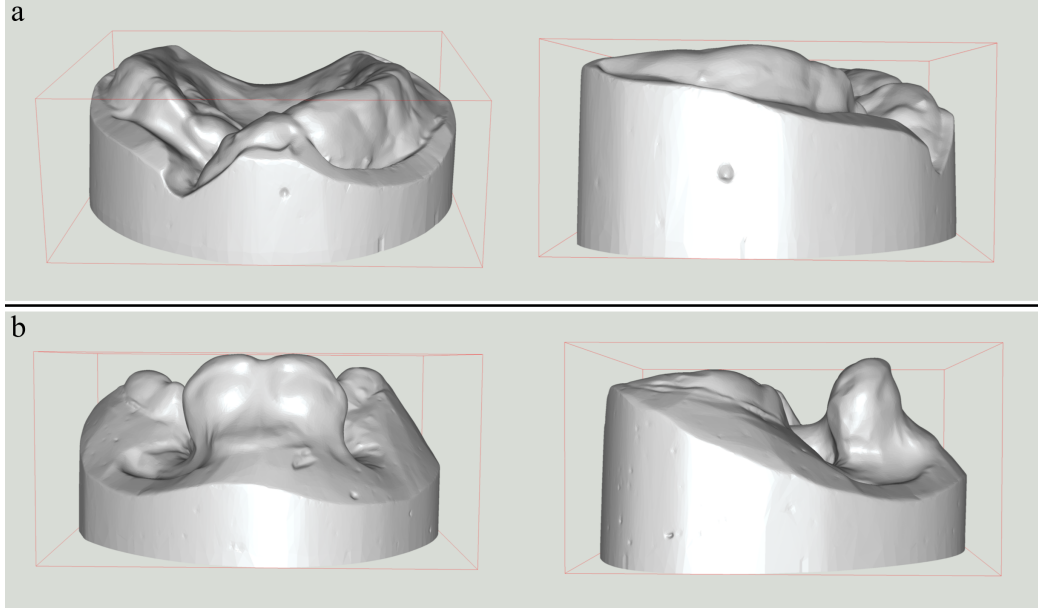


Figure 5: Oriented bounding box of two cleft models

segment count is either 2 or 3 (corresponding to 1 or 2 gaps), the number of peaks is also limited to 2 or 3. Based on their orientation, we designate these peaks as the left, right, and forward peaks, denoted as \mathbf{P}_l , \mathbf{P}_r and \mathbf{P}_f respectively (See Figure 8). The height of a point is defined as:

$$\text{height}(\mathbf{p}) = \text{dot}(\vec{\mathbf{u}}_{\text{up}}, \mathbf{p} - \mathbf{o}) \quad (2)$$

where \mathbf{p} represents a point on the model, and \mathbf{o} denotes the origin of the local coordinate system.

The left and right peaks \mathbf{P}_l , \mathbf{P}_r always exist; however the forward peak \mathbf{P}_f may be absent in the case of a unilateral cleft. Initially, our approach assumes that three peaks are all present (see Figure 7, third image). Then these peaks serve as the starting points, or seeds, for the region-growing algorithm described in Section 3.3. If the model is determined to be unilateral, the forward peak \mathbf{P}_f will be removed.

To locate the initial three seeds (peaks), we separate the whole model into three regions and find the highest vertex in each region. It is imperative to note that this division serves exclusively for the initial peak determination and does not influence the subsequent propagation process of the region-

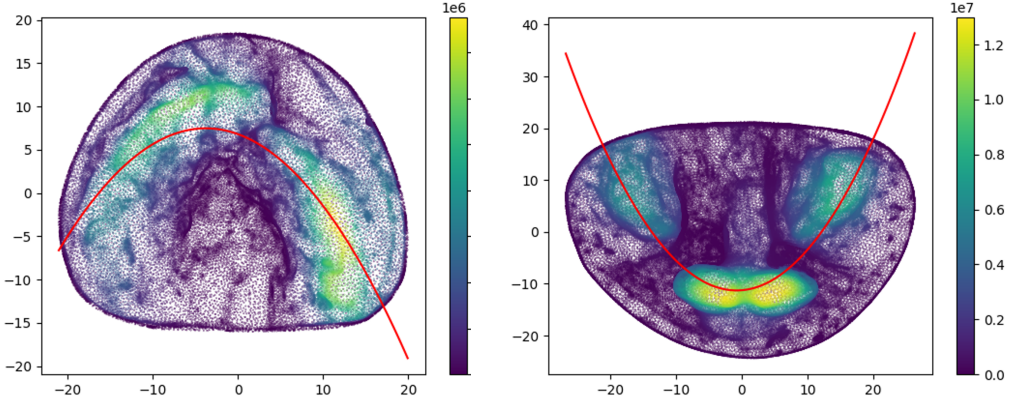


Figure 6: Quadratic fitting with a color-weighted map to assess the direction of the forward unit vector. In the left image, the \cup shape (positive x^2 coefficient) indicates that the forward direction is actually reversed and requires correction.

growing algorithm. These regions, illustrated in Figure 8, are delineated as follows:

- \mathbf{R}_l : Extends more than λ mm to the left of the origin.
- \mathbf{R}_r : Extends more than λ mm to the right of the origin.
- \mathbf{R}_f : Covers areas within λ mm on either side of the origin and extends more than λ mm to the forward of the origin.

The parameter λ is adjustable; Experimental results shows $\lambda = 10$ proved effective for most models

3.3. Recognize the alveolar segments

With the three peaks identified, we use them as initial seeds to perform the region-growing process. The resulting spread provides an approximation of the shapes of the alveolar segments. We then analyze these shapes to determine the number of alveolar segments, allowing us to classify the model as either unilateral or bilateral.

3.3.1. Stopping criterion

Due to the substantial variation in the size and morphology of alveolar clefts, defining an effective stopping criterion for region-growing to accurately

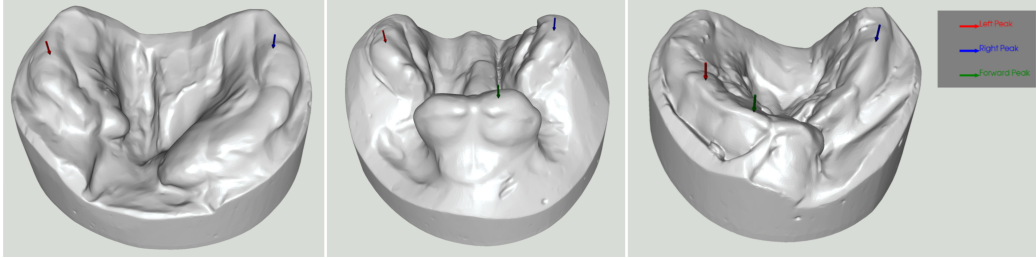


Figure 7: Landmark peaks on different dental models. The third image illustrates the initial three peaks (left, right, and forward) used as seed points for the region-growing process. If the model is classified as unilateral during region growing, the forward peak will be excluded.

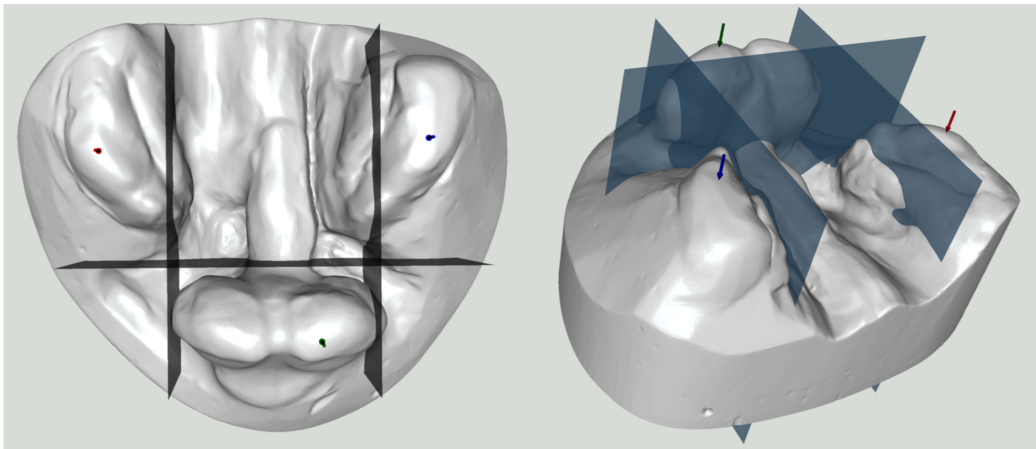


Figure 8: The separated regions in a dental model

capture the boundaries of each alveolar segment is challenging. To address this, we adopt a straightforward approach, using height (Defined at Equation 2) as the primary criterion for approximating the shape of an alveolar segment. A single iteration of region-growing starts at a peak and stops once the region reaches a predefined lower height threshold, denoted as β (See Pseudocode 1 for the algorithm). This choice is supported by the observation of significant height variations at the cleft site (refer to Figure 6 for the height scalar field).

3.3.2. Multi-stage region growing and Position classification

To achieve the most accurate representation of alveolar segment shapes, we employ a multi-stage region-growing approach. This involves performing

region-growing in multiple stages, following a specific order, and selecting the best result (See Figure 9 for some results). Let \mathbf{A}_l , \mathbf{A}_r and \mathbf{A}_f represent the regions grown from \mathbf{P}_l , \mathbf{P}_r and \mathbf{P}_f respectively. The approach is guided by the following conditions:

- \mathbf{A}_l and \mathbf{A}_r must not overlap, regardless of whether the case is bilateral or unilateral.
- In the bilateral case, \mathbf{A}_f must not overlap with \mathbf{A}_l and \mathbf{A}_r .
- In the unilateral case \mathbf{A}_f may only overlap with one of \mathbf{A}_l and \mathbf{A}_r .

Based on these conditions, the multi-stage region-growing procedure can be separated into 3 steps:

1. Perform region growing from three peaks dependently using a small $\beta = 2$ mm. If \mathbf{A}_f doesn't overlap with either \mathbf{A}_l or \mathbf{A}_r , Classify the model as bilateral and proceed to step 2. If \mathbf{A}_f overlaps with either \mathbf{A}_l or \mathbf{A}_r , classify the model as unilateral and proceed to step 3.
2. For bilateral cases, perform region-growing from all three peaks using varying β values, starting from a higher value (4.5 mm) and gradually decreasing. If overlap occurs between any two resulting areas, reduce β until no overlap is observed.
3. In unilateral cases, discard the forward peak \mathbf{P}_f and perform region growing from \mathbf{P}_l and \mathbf{P}_r using varying β values starting from a higher value (4.5 mm) and gradually decreasing. If a given β results in overlap between \mathbf{A}_l and \mathbf{A}_r , reduce β until no overlap is observed.

Step 1 determines whether the model is unilateral or bilateral, based on the observation that the depth of a cleft is typically greater than 2 mm. Therefore, with $\beta = 2$ mm, any overlap between the two resulting areas suggests that they belong to the same segment without a clear gap between them. Once the cleft's position has been classified, steps 2 and 3 aim to capture the alveolar segments with maximum precision by iterating through multiple β values. The choice of initial maximum $\beta = 5$ mm is chosen based on experimental results, which will be further discussed in section 5.2

3.3.3. Speeding up and Algorithm

To enhance the algorithm's efficiency, it is important to note that a Mesh comprises not only vertices but also a list of triangles, each defined by the

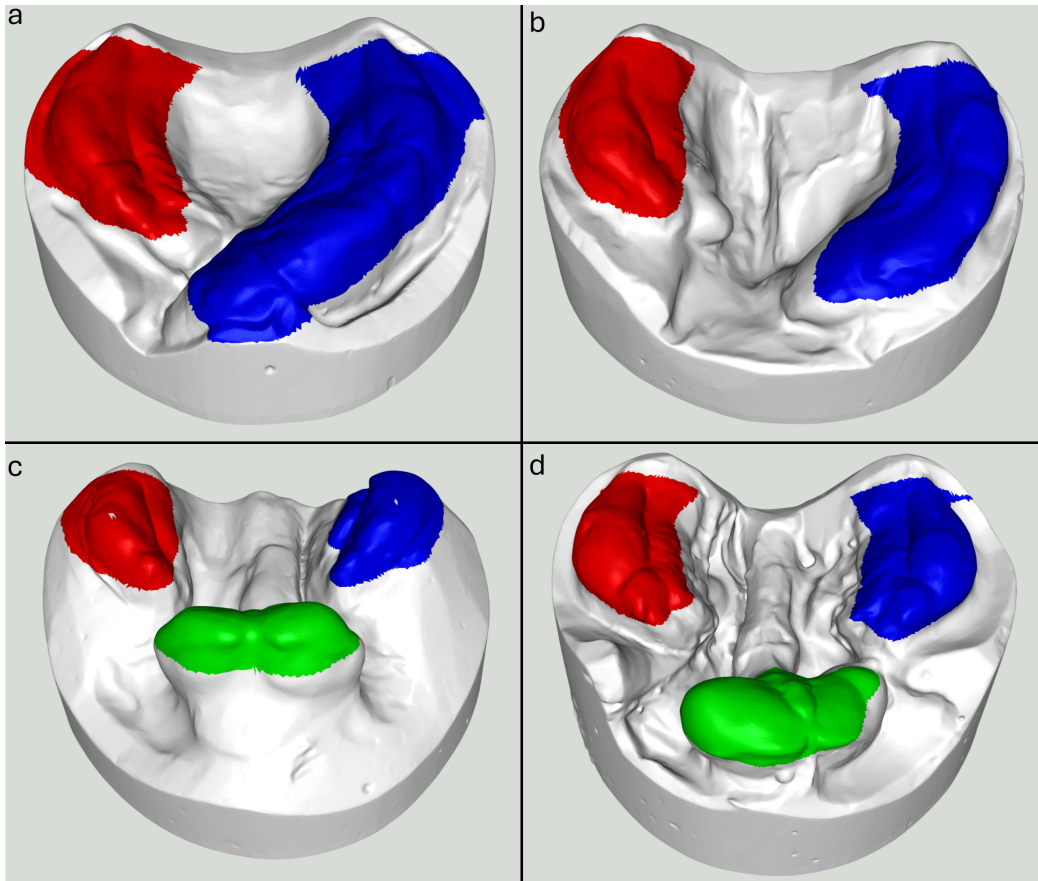


Figure 9: Some Segmentation results on different neonatal dental models. Red, green, and blue regions represent the region-growing results from left, forward, and right peaks. (a) one incomplete cleft. (b) one complete cleft. (c) two complete clefs. (d) one complete cleft and one incomplete cleft.

(X, Y, Z) coordinates of its three vertices. Expanding a region on a point-by-point basis can be inefficient and time-consuming. To address this issue, we adopt a strategy of expanding regions by processing triangles as a unit. This method significantly accelerates the expansion process. The detailed steps of this triangle-based region expansion are outlined in Pseudocode 1, utilizing the following parameters for clarity and efficiency in the algorithm's execution.

- $T[i]$: a boolean flag indicating whether triangle triangle i has been included in the expansion process (with $i \in [0, \text{number of triangles in the model} - 1]$).
- $V[i]$: a boolean flag denoting whether triangle i has been visited during the algorithm's execution.
- β : This parameter represents the height difference below a peak.

3.4. Recognize the clefts (gaps) between alveolar segments

In this section, we describe the process of identifying and analyzing the gaps (clefts) between the previously determined alveolar segments. First, we locate specific landmarks near the gaps. These landmarks are then used to compute the shortest paths between segments, which serve as approximations of the gap shapes. Finally, we analyze the geometry of each shortest path to classify the corresponding cleft as either complete or incomplete. This method is based on the observation that the shortest path inherently passes through the gap, making it a reliable representation of the cleft's shape.

3.4.1. Identify near-gap landmarks and calculate shortest paths

Near-gap landmarks are defined as points located on the edges of the alveolar segments near the cleft regions (See Figure 10). These landmarks are critical for accurately capturing the spatial geometry of the gaps. Depending on the cleft type, the number of landmarks differs:

1. **Bilateral Cases:** Two near-gap landmarks are identified on the left and right alveolar segments, denoted as $\mathbf{NG}_l, \mathbf{NG}_r$.
2. **Unilateral Cases:** Two additional landmarks are identified on the forward alveolar segment, denoted as \mathbf{NG}_f and \mathbf{NG}_{fr} . These, together with $\mathbf{NG}_l, \mathbf{NG}_r$, provide four landmarks for bilateral clefts.

Algorithm 1: A single iteration of region-growing with height threshold as criteria

Data: Peak P , Mesh M
Result: Tag array T

Initialize all $T[i]$ s to 0;
Initialize all $V[i]$ s to 0;
Initialize an empty queue Q ;
/* Add triangles which contain the peak to the queue */
for Triangle t that contains p **do**
 | $Q.push(t);$
 end
 $max_h \leftarrow \text{dot}(\vec{u}_{\text{up}}, P);$
while Q isn't empty **do**
 | $t \leftarrow Q.pop();$
 | **if** $V[t.index] = 1$ **then**
 | | continue ; /* this triangle has been processed */
 | **else**
 | | $V[t.index] \leftarrow 1;$
 | | $h \leftarrow \text{dot}(\vec{u}_{\text{up}}, t.centroid);$
 | | **if** $h < max_h$ and $h > max_h - \beta$ **then**
 | | | $Tag[t.index] \leftarrow 1;$
 | | | /* Add t 's 3 neighbor triangles to the queue */
 | | | **for** Triangle $n \in t.neighbors$ **do**
 | | | | $Q.push(n);$
 | | | **end**
 | | **end**
 | | **end**
 | **end**
end

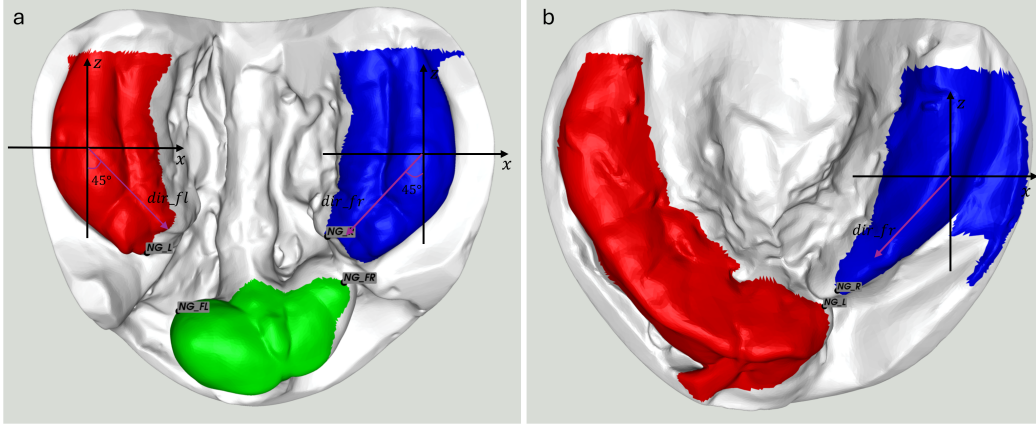


Figure 10: Examples of near-gap landmarks and the directions used to determine them

To identify these landmarks, we use a method similar to the peak-finding process. Specifically:

- The maxima (farthest points) on each segment are determined along predefined directional vectors. These directions are approximated based on the extension of the segment boundaries (See Figure 10):
 - **dir_f** : The forward direction rotated 45 degrees counterclockwise along the Y-axis.
 - **dir_{fr}** : The forward direction rotated 45 degrees clockwise along the Y-axis.
- Distances along these directions are calculated using the dot product, similar to the calculation of height in the peak-finding process.

Once the landmarks are identified, we compute the shortest paths between them using Dijkstra's algorithm, which effectively finds the optimal path on a 3D surface (See Figure 11, 12). The shortest paths are calculated as follows:

- **Bilateral Cases:** Compute the shortest path between **NG_l** and **NG_r**.
- **Unilateral Cases:** Compute the shortest path between **NG_l** and **NG_f**, as well as between **NG_r** and **NG_{fr}**

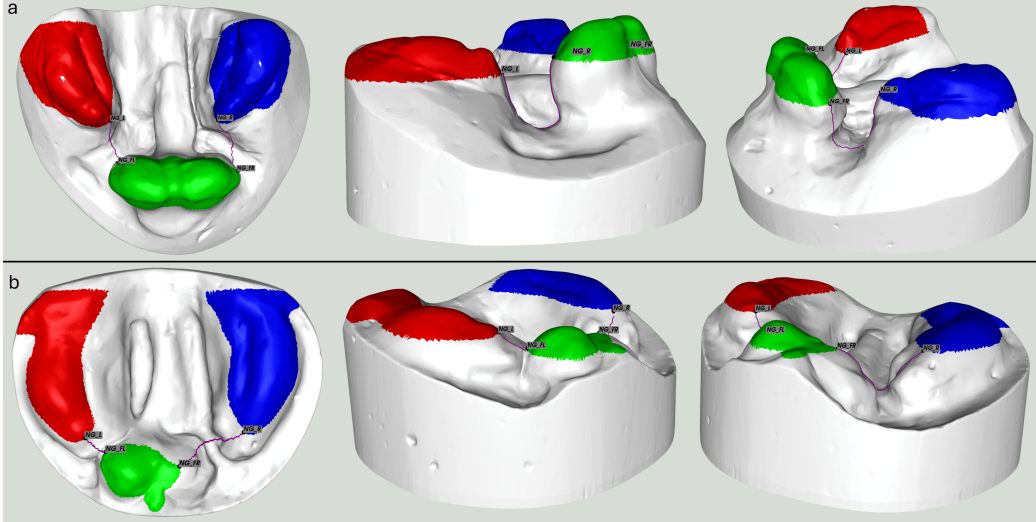


Figure 11: Near-gap landmarks and shortest paths (purple lines) on two bilateral cleft models. In model (a), both clefts are complete, whereas in model (b), one cleft is complete and the other is incomplete.

3.4.2. Classify cleft’s completeness

To classify clefts as complete or incomplete, we analyze the geometry of the shortest paths, focusing on two key attributes: **width** and **depth**. These attributes serve as approximations of the cleft’s physical dimensions:

- **Width:** The horizontal distance between the endpoints of the shortest path, measured along the direction connecting the two endpoints.
- **Depth:** The vertical distance between the lowest point along the path and the smaller height of the two endpoints, measured along the \vec{u}_{up} direction. This ensures that the depth of the cleft is relative to the endpoints.

The underlying rationale is that complete clefts tend to be both wider and deeper than incomplete clefts. Let T_d and T_w denote the **height threshold** and **depth threshold**, respectively. Based on experimental results:

- $T_d = 4 \text{ mm}$: The cleft is considered sufficiently deep if the depth exceeds 4.

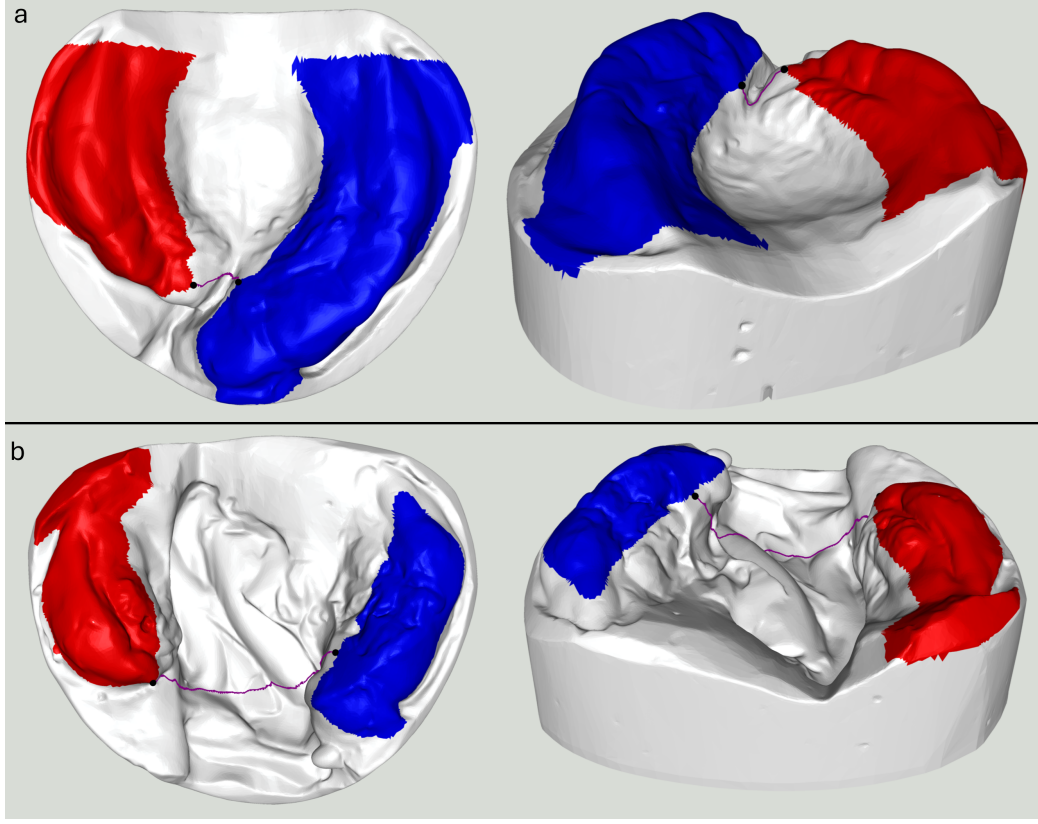


Figure 12: Near-gap landmarks and shortest paths (purple lines) on two unilateral cleft models. Model (a) has an incomplete cleft, whereas model (b) has a complete cleft.

- $T_w = 5 \text{ mm}$: The cleft is considered sufficiently wide if the width exceeds 5

The selection of $T_d = 4 \text{ mm}$ and $T_w = 5 \text{ mm}$ are based on the experimental results. Using these thresholds, the classification criteria are as follows:

- A cleft is classified as **complete** if both the width and depth exceed T_h and T_w , indicating a significant gap.
- A cleft is classified as **incomplete** if either the width or depth falls below T_h and T_w , suggesting partial connectivity between segments.

4. Results

Using our method, we correctly classified 15 out of 17 neonatal dental models (88 %) as shown in Table 1. 5 successful results have been demonstrated in the previous sections (See Figure 4, 11, 12). Figure 14 showcases 4 additional successful results. These 8 models of varying complexity together demonstrate the effectiveness and robustness of our method. The 2 failed cases will be discussed in Section 5.

We also recorded the time consumption of our approach on different scales of dental models (measured with the number of mesh points and triangles) during experiments, as shown in Figure 13, including the time for (a) computing OBB and determining orientation, (b) multi-stage region growing, (c) computing the shortest paths, and (d) total time for classification. All experiments were carried out on a common PC with Intel Core i7-8700 Processor 3.20 GHz with 16 GB memory.

The results indicate that the most time-intensive step was multi-stage region growing, as it involves iterative processes with varying β values to ensure precision. The number of iterations is inversely proportional to the depth of the clefts, as the algorithm decreases β from a higher value.

5. Discussions

This section discusses the failed cases and highlights some key challenges that require further resolution.

5.1. Orientation

Our orientation method using an oriented bounding box is more effective and reliable than PCA-based methods (Figure 15). This technique is highly adaptable and can be applied to various dental models, not only neonatal dental models. However, it does have some limitations.

The OBB-based orientation process primarily depends on the model's non-biometric base rather than its biometric surfaces. This non-biometric base can either be a plaster foundation or an addition generated by post-processing software. The preparation of these bases often varies due to differing trimming or processing practices. A key limitation of this method is the reliance on the base having specific dimensions: it must be wider (left/right) than it is long (forward/backward) and longer than it is tall. When these dimensional requirements are not met, the orientation results can be inaccurate.

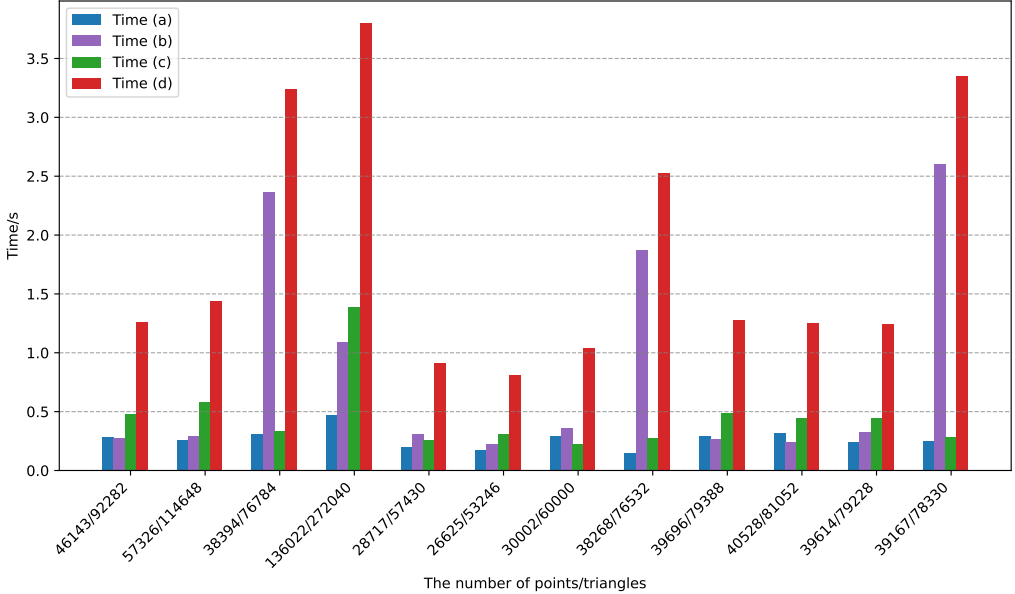


Figure 13: Time statistics of our alveolar cleft classification. The timing is recorded in seconds for (a) orientation determination, (b) multi-stage region growing, (c) shortest paths computation, and (d) total time of classification.

Future research on the orientation of neonatal dental models could focus on utilizing biometric surfaces rather than relying on non-biometric bases. Additionally, developing methods capable of processing non-watertight models would eliminate the need for a base altogether. This approach would not only reduce uncertainties in orientation but also save time and labor costs, making the process more efficient and reliable.

5.2. Region-growing and segmentation

Our region-growing algorithm, which uses height as the key stopping criterion, effectively partitions and recognizes the alveolar segments through a multi-stage process. However, the segmentation outcomes are sensitive to the initial selection of β value. A small β value often results in insufficient expansion, failing to accurately approximate an alveolar bone segment. Conversely, a slightly larger β value can lead to overgrowth, where regions expand beyond their intended boundaries and encroach upon surrounding noise surfaces, such as cheek soft tissue and the plaster base. In our study, the only two models that failed classification were due to such overgrowth

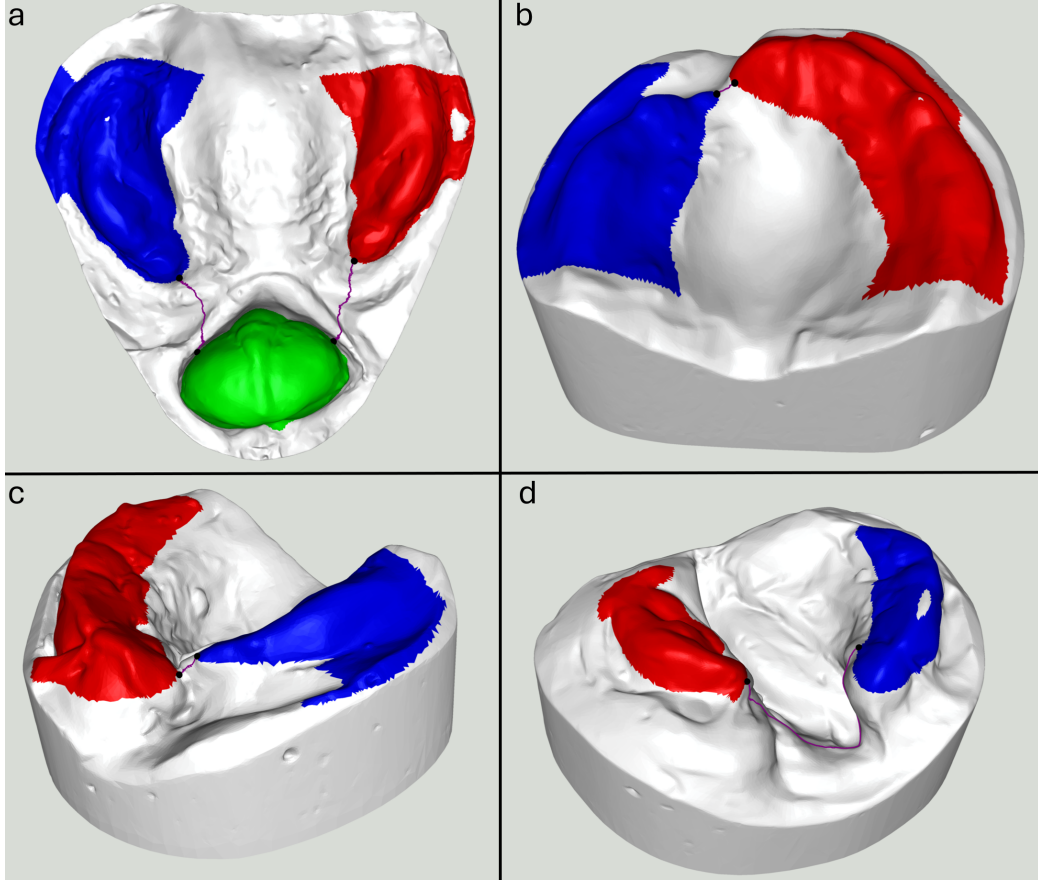


Figure 14: 4 successful results of our approach. (a) 2 complete clefts (b) 1 incomplete cleft. (c) 1 incomplete cleft. (d) 1 complete result.

with $\beta = 4.5$, which led to incorrect identification of near-gap landmarks, as shown in Figure 16. However, with a smaller β value, the expansion remains within the cleft boundary, resulting in correct classification for these two cases.

This observation highlights the challenge of determining a universally optimal β value for all models. Experimental evaluations suggest that a β value of 4.5 performs well across the majority of tested models. However, variability in model characteristics, such as differences in alveolar bone height and plaster base dimensions, makes it impractical to rely on a single fixed value for all cases.

One potential improvement to the algorithm is the incorporation of an

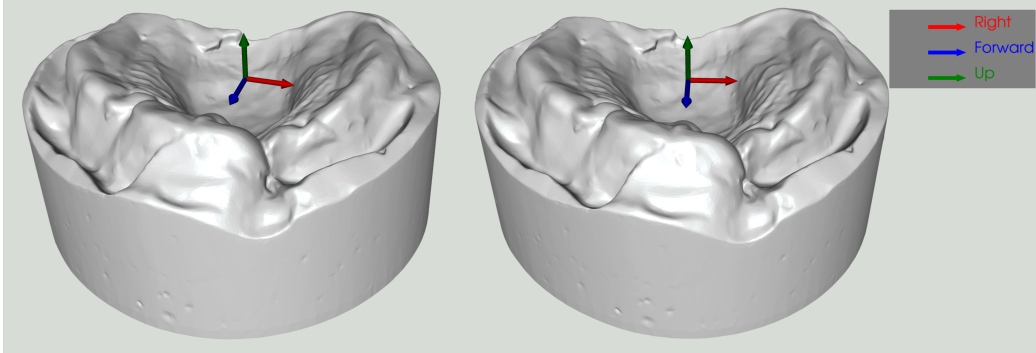


Figure 15: Orientation results by PCA (Left) and OBB(Right)

adaptive mechanism for selecting β based on the specific characteristics of each model. This approach could dynamically adjust β to better suit individual models, reducing the likelihood of overgrowth. Additionally, refining the segmentation results by eliminating the plaster base through curvature-based analysis could further enhance accuracy. These improvements would address current limitations and contribute to more robust and reliable segmentation outcomes.

6. Conclusions

We developed from scratch a set of methods for automated cleft classification on 3D neonatal dental surfaces. By leveraging biometric features and computational geometry, our methods effectively segment alveolar bone regions and classify clefts as unilateral or bilateral and as complete or incomplete. The complex and unpredictable geometry of alveolar clefts necessitates original and innovative methods, which are not readily available in existing literature.

Our methods include the following steps:

1. Use the centroid of the mesh, an oriented bounding box, and a quadratic fit to the alveolar bone to determine an approximate position and orientation of the neonatal dental mesh.
2. Identify the maxima in the vertical direction to automatically locate the highest points (peaks) on each alveolar segment.
3. Perform multi-stage region-growing, using the identified peaks as initial seeds, to segment the alveolar bone into distinct regions. Classify

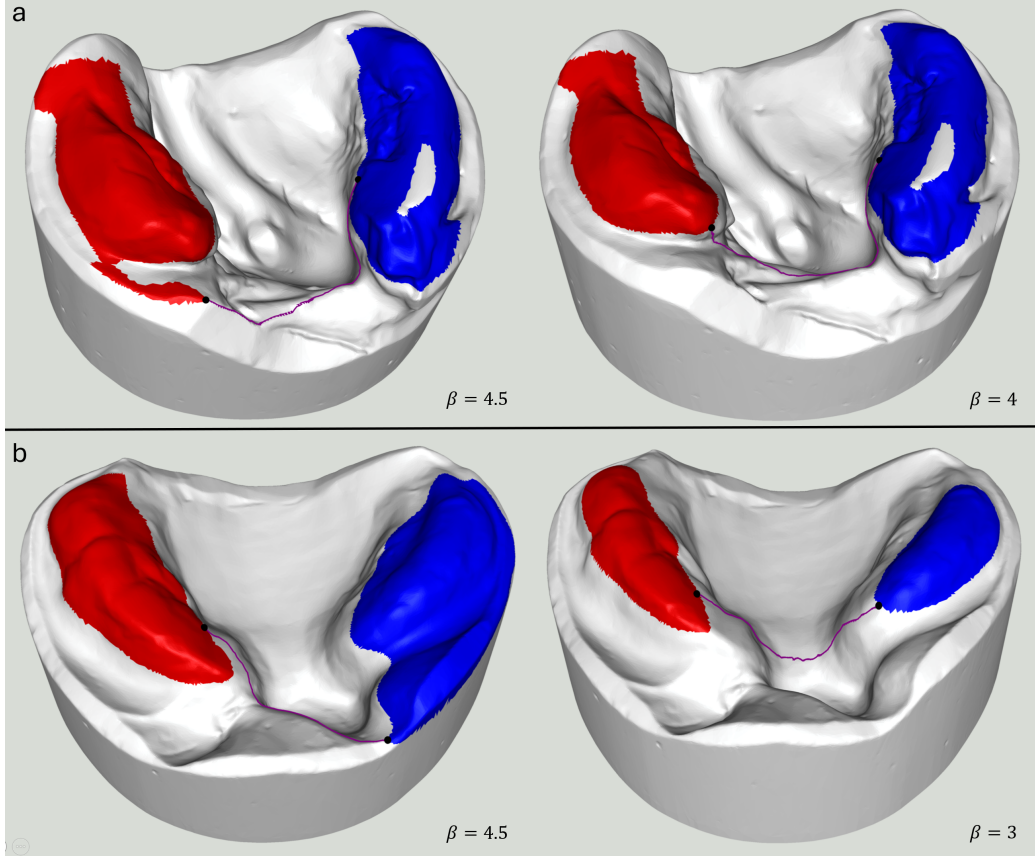


Figure 16: The only 2 failed cases in the classification process. For both models, a $\beta = 4.5$ caused the region-growing results to overgrow into the surrounding plaster base, leading to incorrect identification of near-gap landmarks. However, using $\beta = 4$ for model(a) and $\beta = 3$ for model(b) resulted in successful classification.

the model as unilateral or bilateral based on the spatial relationship between these regions.

4. Locate near-gap landmarks on the segmented alveolar regions to approximate the positions of the clefts. For bilateral cases, additional landmarks are identified on the forward alveolar segment.
5. Compute the shortest paths between near-gap landmarks using Dijkstra's algorithm. These paths are used to approximate the shape and extent of the clefts.
6. Analyze the geometry of the shortest paths, specifically their width and height, to classify each cleft as complete or incomplete.

We also discuss the limitations of our approach, including the dependency on non-biometric bases for orientation and the challenges of segmenting complex geometries, while proposing directions for future research.

Overall, this automated method represents a significant step forward in the clinical and research management of neonatal cleft cases. It offers a promising solution for reducing reliance on manual assessment, improving accuracy, and accelerating the classification process, thereby contributing to better patient outcomes and streamlined workflows in dental practice.

Appendix A. Example Appendix Section

Statement

During the preparation of this work, Yihang Xie used OpenAI’s ChatGPT in order to enhance the readability and language of the manuscript. After using this tool, Ping Lin and Peter Mossey carefully reviewed and edited the content as needed and take full responsibility for the content of the published article.

References

- [1] P. Mossey, B. Modell, Epidemiology of oral clefts 2012: an international perspective, *Cleft lip and palate* 16 (2012) 1–18.
- [2] O. Kriens, Lahshal: a concise documentation system for cleft lip, alveolus, and palate diagnoses, *What is a cleft lip and palate* (1989) 32–3.
- [3] W. McBride, G. McIntyre, K. Carroll, P. Mossey, Subphenotyping and classification of orofacial clefts: need for orofacial cleft subphenotyping calls for revised classification, *The Cleft Palate-Craniofacial Journal* 53 (5) (2016) 539–549.
- [4] K. H. Wang, C. L. Heike, M. D. Clarkson, J. L. Mejino, J. F. Brinkley, R. W. Tse, C. B. Birgfeld, D. A. Fitzsimons, T. C. Cox, Evaluation and integration of disparate classification systems for clefts of the lip, *Frontiers in physiology* 5 (2014) 163.
- [5] P. A. Mossey, J. Little, R. G. Munger, M. J. Dixon, W. C. Shaw, Cleft lip and palate, *The Lancet* 374 (9703) (2009) 1773–1785.

- [6] S. Tian, N. Dai, B. Zhang, F. Yuan, Q. Yu, X. Cheng, Automatic classification and segmentation of teeth on 3d dental model using hierarchical deep learning networks, *Ieee Access* 7 (2019) 84817–84828.
- [7] B.-j. Zou, S.-j. Liu, S.-h. Liao, X. Ding, Y. Liang, Interactive tooth partition of dental mesh base on tooth-target harmonic field, *Computers in biology and medicine* 56 (2015) 132–144.
- [8] B. Woodsend, E. Koufoudaki, P. A. Mossey, P. Lin, Automatic recognition of landmarks on digital dental models, *Computers in Biology and Medicine* 137 (2021) 104819.
- [9] Y. Kumar, R. Janardan, B. Larson, Automatic feature identification in dental meshes, *Computer-Aided Design and Applications* 9 (6) (2012) 747–769.
- [10] X. Ma, C. Martin, G. McIntyre, P. Lin, P. Mossey, Digital three-dimensional automation of the modified huddart and bodenham scoring system for patients with cleft lip and palate, *The Cleft palate-craniofacial journal* 54 (4) (2017) 481–486.
- [11] T. Kronfeld, D. Brunner, G. Brunnett, Snake-based segmentation of teeth from virtual dental casts, *Computer-Aided Design and Applications* 7 (2) (2010) 221–233.
- [12] J. O'Rourke, Finding minimal enclosing boxes, *International journal of computer & information sciences* 14 (1985) 183–199.
- [13] S. Gottschalk, M. C. Lin, D. Manocha, Obbtree: A hierarchical structure for rapid interference detection, in: *Proceedings of the 23rd annual conference on Computer graphics and interactive techniques*, 1996, pp. 171–180.
- [14] G. Barequet, S. Har-Peled, Efficiently approximating the minimum-volume bounding box of a point set in three dimensions, *Journal of Algorithms* 38 (1) (2001) 91–109.
- [15] C.-T. Chang, B. Gorissen, S. Melchior, Fast oriented bounding box optimization on the rotation group $so(3, \mathbb{R})$, *ACM Transactions on Graphics (TOG)* 30 (5) (2011) 1–16.

- [16] The CGAL Project, CGAL User and Reference Manual, 5.6 Edition, CGAL Editorial Board, 2023.
URL <https://doc.cgal.org/5.6/Manual/packages.html>
- [17] E. Kalogerakis, A. Hertzmann, K. Singh, Learning 3d mesh segmentation and labeling, ACM Trans. Graph. 29 (4) (Jul. 2010). doi:10.1145/1778765.1778839.
URL <https://doi.org/10.1145/1778765.1778839>
- [18] Y. He, H. Yu, X. Liu, Z. Yang, W. Sun, A. Mian, Deep learning based 3d segmentation: A survey, arXiv preprint arXiv:2103.05423 (2021).
- [19] R. S. Rodrigues, J. F. Morgado, A. J. Gomes, Part-based mesh segmentation: a survey, in: Computer Graphics Forum, Vol. 37, Wiley Online Library, 2018, pp. 235–274.
- [20] B. Chazelle, D. P. Dobkin, N. Shouraboura, A. Tal, Strategies for polyhedral surface decomposition: An experimental study, in: Proceedings of the eleventh annual symposium on Computational geometry, 1995, pp. 297–305.
- [21] A. P. Mangan, R. T. Whitaker, Partitioning 3d surface meshes using watershed segmentation, IEEE Transactions on Visualization and Computer Graphics 5 (4) (1999) 308–321.
- [22] T. Yuan, W. Liao, N. Dai, X. Cheng, Q. Yu, Single-tooth modeling for 3d dental model, International journal of biomedical imaging 2010 (1) (2010) 535329.
- [23] E. W. Dijkstra, A note on two problems in connexion with graphs, Numer. Math. 1 (1) (1959) 269–271. doi:10.1007/BF01386390.
URL <https://doi.org/10.1007/BF01386390>
- [24] D. Sieger, M. Botsch, The polygon mesh processing library, <http://www.pmp-library.org> (2019).